


## Research Article

# Rydberg Excitation in Infrared-Laser-Pulses Using a Stiffness Reducing Spectral Approach

Rolf Gersbacher<sup>\*</sup>, John T. Broad<sup></sup>

Faculty Management and Technology, University of Applied Sciences Esslingen, Esslingen, Germany  
E-mail: [Rolf.Gersbacher@hs-esslingen.de](mailto:Rolf.Gersbacher@hs-esslingen.de)

**Received:** 13 February 2025; **Revised:** 24 March 2025; **Accepted:** 2 April 2025

**Abstract:** An effective spectral method based on square-integrable ( $L^2$ ) functions is presented to solve the Time-Dependent Schrödinger Equation (TDSE) of an atom in the presence of a strong, rapidly oscillating laser field. The corresponding system of differential equations is extremely stiff. To reduce this problem, the wave function is expanded in an eigenvector basis to the unperturbed atomic Hamiltonian operator and highly oscillating eigenvectors are excluded. An explicit solution method is used for the time propagation, which significantly reduces the demands on Information Technology (IT) resources compared to implicit methods. To avoid numerical reflections due to a finite eigenvector basis, a Complex Absorbing Potential (CAP) is implemented, which is adapted to the  $L^2$  function space. The absorption properties of the CAP are investigated. The method is applied to the ionization and excitation of atomic  $H$  in few cycle laser fields. The Rydberg excitation spectrum after the passage of a laser pulse is calculated and discussed. The results show a pronounced dependence of the Rydberg occupation probabilities on the laser parameters and allow selective control.

**Keywords:** TDSE, stiffness, Coulomb-Sturmians,  $L^2$  expansion, tunnel ionization

**MSC:** 65L05, 34K06, 34K28

## 1. Introduction

The TDSE is the method of choice to describe the interaction of radiation with atoms and to make quantitative statements about observables. The ‘exact’ numerical solution is often used as a reference, for example to validate classical and semiclassical methods such as the Strong Field Approximation (SFA) within the framework of the Simple Man Model [1].

The interaction of intense laser fields in the atto- and femtosecond range leads to excitation and ionization, whereby the continuum electron can travel great distances from the nucleus. The associated wave function can cover spatial ranges of several 100 atomic units (au). However, the ‘exact’ numerical solution of the TDSE is costly, especially for longer interaction times and large radial distances of the electron from the ion body. In addition, the ‘full’ numerical solution of the TDSE for multi-electron systems cannot be realized even today without reducing the spatial dimensionality, e.g. a two-electron system such as He in the  $(6 + 1)$ -dimensional configuration space including time currently represents the limit of what is feasible. Methods such as time dependent density functional theory reduce the dimensionality of the

configuration space by replacing the many-body wave function with a time-dependent averaged electron density. In the limiting case of a time-independent electron density, this leads to the Single Active Electron (SAE) approximation, in which a photoactive electron moves in a static potential averaged over the other electrons.

The solution methods for discretizing the configuration space can be divided into two categories: In finite difference methods, the spatial coordinates and derivatives are sampled by small step sizes and the resulting sparse matrix system is solved per time step. In spectral methods, the solution is expanded according to time-independent basis functions  $F_j(r)$ :  $\Psi = \sum_j a_j(t) F_j(r)$  with time-dependent coefficients  $a_j(t)$ , which are also referred to as spectral representation in analogy to the discrete Fourier expansion. Spectral methods are always to be preferred if the solution is given by a smooth function and are the subject of actual research [2–4]. Using a spectral approach, the TDSE can be converted into a 1st order differential equation system using weighted residuals methods such as the Galerkin method. Compared to finite difference methods, the dimension of this system of equations is significantly reduced. The basis functions are chosen so that they are infinitely often differentiable and square-integrable. The spatial derivatives can then be calculated analytically and do not have to be approximated, as is the case with finite difference methods.

A combination of spectral and difference methods are the Discrete Variable Representation (DVR) methods. In the case of Coulomb scattering, the Coulomb-Wave-DVR [5] has established itself as an alternative to pure spectral methods. Here, the solution function is calculated on selected grid points according to an orthonormal basis. However, the underlying basis functions must be calculated numerically in advance, which significantly increases the effort involved. Similar to spectral methods, the number of grid points can be remarkably reduced compared to finite difference methods. In spectral methods the underlying basis functions are decisive for their quality. In scattering theory at a central potential, Coulomb-Sturmians have proven to be the method of choice alongside Gauss-Hermite and Slater functions. Coulomb-Sturmians are very similar to the bound radial hydrogen functions; they already contain a substantial part of the solution structure for the atomic Hamilton operator and does not have to be built up by a possibly very large combination of basis functions. Fourier-transformed Coulomb-Sturmians in momentum space are also used to solve the TDSE in laser fields [6]. There, three times as many momentum-transformed Coulomb Sturmians per partial wave are required for converged results as in this work.

A spectral approach with a Coulomb-Sturmian basis in the SAE approximation is also adopted in this work. Sturmian functions for the radial coordinate can not only be used to represent bound states, they are also suitable for the approximate representation of continuum states [7, 8]. Together with a partial wave expansion, the  $L^2$  basis transforms the TDSE into a coupled 1st order differential equation system in time, where no more derivatives appear in the spatial domain. However, laser interaction times in the femtosecond range lead to radial excursion amplitudes that require a large number of Sturmians and high partial waves. Sturmian functions approximate the radial geometry of the undisturbed atomic single-electron system, but are also suitable for successfully describing phenomena in laser fields of  $10^{15}$  W/cm<sup>2</sup> [9, 10]. The underlying system is described by the Hamilton operator  $H = H_0 + V(t)$  and is composed of the time-independent atomic component  $H_0$  and a time-dependent external field  $V$ . The spectrum of  $H_0$  consists of the bound states and the upward unbounded continuum states. With increasing basis size  $N$ , higher and higher eigenvalues  $E_j$  are approximated, which leads to a highly oscillating system of differential equations in time. If the external field is ignored, the time behavior is proportional to  $e^{-iE_j t}$ . In order to resolve these highly oscillating states, correspondingly small step sizes  $h$  are required in the time domain:  $h < 1/|E_{max}|$ , where  $E_{max}$  denotes the highest eigenvalue. The problem is exacerbated by the fact that the spectrum has an accumulation point at 0. The ratio  $|E_{max}|/|E_{min}|$  approaches infinity with increasing basis size and is composed of components whose time behavior varies in different orders of magnitude: The corresponding coupled differential equation system is extremely stiff. With explicit time propagation methods,  $\Psi(t_{n+1}) = H(t_n, t_{n-1}, t_{n-2}, \dots, \Psi(t_n), \Psi(t_{n-1}), \dots)$ , the solution  $\Psi(t_{n+1})$  at time  $t_{n+1}$  results from the past values of  $H$ , i.e. the right-hand side does not depend on the current value  $t_{n+1}$ . To avoid numerically no longer manageable stepwidth, implicit propagation methods such as Adams-Moulton or implicit Runge-Kutta methods can help [11, 12]: In implicit methods, the right-hand side of the propagation algorithm  $\Psi(t_{n+1}) = H(t_{n+1}, t_n, t_{n-1}, \dots, \Psi(t_{n+1}), \Psi(t_n), \dots)$  also depends on  $t_{n+1}$ . The numerical effort increases and with it the computer resources required: an additional (linear) system of equations for the expansion coefficients  $a_j(t_{n+1})$  must now be solved for each time step. Longer interaction times and the associated larger radial extensions and occupation of higher partial waves are a challenging task. Test calculations have

shown that when using a Sturmian basis, the stiffness problem is so pronounced that even implicit methods of lower order, such as Adams-Moulton methods, did not result in any improvement. In [13], a predictor-corrector method is used for this purpose; a Runge-Kutta method of order 7 is applied for the corrector, whereby the matrix iterations are parallelized over several Central Processing Unit (CPU) cores per time step.

The same stiffness problem was also shown in the work of [14], which uses a Sturmian basis as well and employs a method developed by Fatunla [15, 16]. An interpolation function is calculated recursively at each time step, which approximates the solution in the time step  $\Psi(t_{n+1})$ . The advantage is that the entire Hamilton operator consisting of  $H_0$  and the external field  $V$  is included in the interpolation and the stiffness caused by high field strengths in the interaction term is also taken into account. Other methods used to calculate the time evolution are Krylov subspace methods such as Arnoldi or Lanczos propagation methods. Here, too, the stiffness problem is evident in the space of Krylov eigenvectors. In [17], the Krylov eigenvectors with the highest eigenvalues are excluded from the propagation, thus eliminating highly oscillating components in the Krylov space. A combination of finite element methods and elimination of eigenvectors with high eigenvalues is also chosen in [18] to reduce the stiffness problem.

Stiff coupled differential equations occur in spectral methods wherever the eigenvalues of the operators involved are unrestricted upwards. In this work, the wave function is therefore represented in a spectral basis of the field-free atomic system and the strongly oscillating eigenvectors are removed from the expansion. This decision is based on the assumption that high-energy continuum states, which are to be regarded as the cause of the stiffness problematic, are not reached during the entire interaction period, i.e. it is assumed that even during the time propagation a virtual excitation into high positive energy states only plays a subordinate role. The results in the following section show that this assumption is justified and can reduce - but not eliminate - the stiffness problem. A suitable explicit time method can subsequently be used for time propagation, which makes additional matrix operations per time step superfluous, as is the case with implicit methods.

During the interaction time, the electron can penetrate into regions of space far away from the nucleus, which requires a large number of basis functions or large lattices. The simplest option is to choose the radial extension and thus the basis so large that this limit is not reached at any time during propagation. Of course, this is in conflict with finite computer resources. The border of the configuration space or the  $L^2$  function space represents a hard, reflective, wall that leads to unphysical reflections that are superimposed on the outgoing waves. It is therefore desirable to set up boundary conditions reducing the reflection and having an absorbing effect. The exterior complex scaling method [19, 20] or the insertion of a Complex Absorbing Potential (CAP) or damping terms at the border of the configuration space are used as standard methods. Other methods include time-dependent scaling of the radial coordinate [17], but also absorption methods that embed the asymptotic behavior of the wave function in the coupled differential equation system. In [9], for example, the authors fitted the Coulomb asymptotics of the field-free solution into the system of equations for the transition amplitudes. In the case of a Sturmian basis, the asymptotics can be represented by Pollaczek functions, which additionally leads to a nonlinear system of equations for the absorption frequencies for each time step and partial wave. For a large basis, the calculation of the Pollaczek functions and the associated determination of the zeros is very time-consuming. Therefore, this approach is not taken here and instead a modified version of a complex absorbing potential is used. The CAP is a universal method and requires no knowledge of the structure of the solution or the asymptotic behavior. It can be directly included as an operator in the Hamiltonian without setting further equations for the boundary conditions. The CAP is an anti-hermitian and time-independent term whose matrix values in an  $L^2$ -basis must be calculated once before propagation and can therefore be used for all time steps. In this work, an alternative approach for the CAP is applied, which, in contrast to the predominant use, is not placed in the configuration space, but at the boundary in the function space.

The objective of the article is twofold:

- To assess how well the  $L^2$ -spectral method can produce reliable results in terms of the CAP-damping behaviour, the stepwidth and the basis size.
- To simulate excitation processes of atomic hydrogen in intense low frequency fields: After transition to the continuum, the electron is backscattered by the external electric field superimposed on the Coulomb field and finally trapped in a Rydberg state. This process is not directly accessible using the SFA of the Simple Man's Model and is currently also being investigated by other groups [21–30]. By utilizing a Coulomb-Sturmian basis, the spectral approach allows for a precise representation of the wavefunction, facilitating the analysis of Rydberg excitations in atomic hydrogen.

In particular, this enables a detailed investigation of the Rydberg spectrum as a function of central laser parameters such as the Carrier Envelope Phase (CEP), intensity, and number of oscillation cycles and thus allows a deeper understanding of the ionization dynamics in intensive laser fields.

To this purpose, the spectral representation in a Sturmian basis is first explained and the explicit propagation method used is presented. Then the  $L^2$  implementation of the CAP is described. The numerical results are then analyzed and subsequently excitation processes are investigated.

In the following, atomic units (au) are used.

## 2. Theory

When using spectral methods, the selection of a suitable basis in which the wave function is represented, is of crucial importance. From the viewpoint of completeness, the different basis sets are equivalent. However, this is not the case when the numerical implementation is concerned with criteria such as CPU runtime and memory usage. Sturmian functions have been established and proven in time-independent scattering theory such as J-Matrix theory or the Convergent Close Coupling method and are also used to describe time-dependent phenomena as an alternative to finite difference methods or B-spline methods. Further developments are also the ‘Generalized Sturmian Functions’ [31], where functions with incoming or outgoing wave asymptotics are numerically calculated utilizing a Sturmian basis. The approach with Coulomb-Sturmians to cover the radial configuration space is also used here and explained in this chapter. For this purpose, the  $L^2$  expansion and the associated differential equation system are presented, the formulation of the CAP in the  $L^2$  function space, the propagation method and the extraction of physical observables follow.

### 2.1 Expansion in atomic eigenstates

If an atom is exposed to a laser field, the temporal development is described by the TDSE:

$$H \Psi(\vec{r}, t) = (H_0(\vec{r}) + V(\vec{r}, t) - i\eta W) \Psi(\vec{r}, t) = i \frac{\partial}{\partial t} \Psi(\vec{r}, t). \quad (1)$$

The Hamiltonian operator consists of three components:  $H_0$  describes the atomic system

$$H_0 = -\frac{1}{2} \vec{\nabla}_r^2 + U_{eff}(r), \quad (2)$$

with an effective potential  $U_{eff}$ , for which the Coulomb potential to the nuclear charge  $Z = 1$ ,  $U_{eff} = Z/r$ , is used in this work. The term  $V$  describes the interaction of the external field with the atom; the dipole approximation in the length form with linear polarization in the  $z$  direction,  $\vec{\epsilon} = (0, 0, z)$ , is applied:

$$V(\vec{r}, t) = \vec{r} \cdot \vec{\epsilon} E(t). \quad (3)$$

The relationship with the vector potential  $\vec{A}$  is  $\vec{E}(t) = -d\vec{A}(t)/dt$ , which - to enable comparisons with other work - is expressed in the form

$$\vec{A}(t) = \frac{E_0}{\omega} \sin^2\left(\frac{\pi t}{T_f}\right) \sin(\omega t + \phi) \vec{\epsilon}. \quad (4)$$

$E_0$  symbolizes the peak amplitude of the laser field,  $\omega$  its frequency, the  $\sin^2$  term describes the enveloping waveform,  $T_f$  the duration of the interaction pulse and  $\phi$  is a phase factor that characterizes the amplitude relative to the enveloping one: the CEP. This phase factor plays an important role in laser pulses with few oscillation cycles and can be used to control the ionization in addition to the amplitude and frequency. For laser pulses with many oscillation cycles, the CEP becomes irrelevant. The electric field amplitude  $E_0$  is calculated from the peak intensity  $I_p$  by  $E_0 = (I_p/I_0)^{\frac{1}{2}}$  with the atomic intensity unit  $I_0 = 3.509445 \cdot 10^{16}$  W/cm<sup>2</sup>. The term  $-i\eta$  W characterizes the absorbing complex potential term operating at the boundary of the  $L^2$  - function space.

To solve (1), a partial wave expansion is performed in a Coulomb-Sturmian basis, these are given by

$$F_n^l(\vec{r}) = \frac{f_n^l(r)}{r} Y_{lm}(\hat{r}), \quad f_n^l(r) = N_n^l e^{-\xi r/2} (\xi r)^{l+1} L_n^{2l+2}(\xi r), \quad (5)$$

with spherical harmonics  $Y_{lm}$  and Laguerre polynomials  $L_n^{2l+2}$ .  $N_n^l$  denotes a normalization constant and  $\xi$  a parameter that can be chosen to fit the problem, e.g. to set the focus on Rydberg states. Smaller values of  $\xi$  lead to a shift of the maximum to larger radial values, the maximum of  $f_n^l$  is localized approximately at  $\sim 2n/\xi$ . A discussion of the optimum value of  $\xi$  can be found in [13]. The functions  $F$  are orthonormal:

$$\langle F_n^l | F_{n'}^{l'} \rangle = \delta_{nn'} \delta_{ll'}, \quad \text{with } N_n^l = \sqrt{\frac{\xi \Gamma(n+1)}{\Gamma(n+2l+3)}}.$$

In this basis, the radial matrix elements of  $H_0$  can be evaluated analytically,  $\Gamma$  is the Gamma function and  $n_<$  denotes the  $\min(n, n')$ :

$$\begin{aligned} h_{nn'}^l &= \int_0^\infty dr f_n^l \left( -\frac{1}{2} \frac{d^2}{dr^2} + \frac{l(l+1)}{2r^2} - \frac{z}{r} \right) f_{n'}^l \\ &= \frac{\xi}{2} \frac{\Gamma(n_<+2l+3)}{\Gamma(n_<+1)} \left[ \frac{n_<}{2l+3} + \frac{1}{2} - \frac{z}{\xi(l+1)} - \delta_{nn'} \frac{1}{4} \right]. \end{aligned} \quad (6)$$

From the hermiticity of  $H_0$  follows  $h_{nn'}^l = h_{n'n}^l$ . The solution  $\Psi$  is not directly expanded in (5) but according to eigenvectors  $\Psi_j^l$  of  $H_0$ , which result from the diagonalization of  $H_0$  in a finite basis of size  $N$ :

$$\Psi(\vec{r}, t) = \sum_{j=0}^{jmax} \sum_{lm} a_j^{lm}(t) \Psi_j^l(r) Y_{lm}(\hat{r}). \quad (7)$$

The  $\Psi_j^l$  are the eigenvectors to the radial Hamilton operator (6) with eigenenergies  $E_j^l$  and are given through:

$$\Psi_j^l(r) = \sum_{n=0}^{N-1} b_{nj}^l \frac{f_n^l(r)}{r} \quad \text{with } \langle \Psi_j^l Y_{lm} | H_0 | \Psi_{j'}^{l'} Y_{l'm'} \rangle = E_j^l \delta_{jj'} \delta_{ll'} \delta_{mm'}. \quad (8)$$

Projection of (1) onto the eigenvectors  $\Psi_j^l$  (8) leads to a coupled system of differential equations of first order in time

$$\langle \Psi_j^l(r) Y_{lm}(\hat{r}) | H - i \frac{d}{dt} | \Psi(\vec{r}, t) \rangle = 0 \quad (9)$$

$$-i \sum_{j'=0}^{j_{\max}} \sum_{l'm'} \left[ E_j^l \delta_{jj'} \delta_{ll'} + V_{jj'}^{lm'l'm'} (\delta_{l'l-1} + \delta_{l'l+1}) - i\eta W_{jj'}^{ll'} \right] a_{j'}^{l'm'} = \frac{d}{dt} a_j^{lm} \quad (10)$$

The interaction term  $V$  in the eigenvector basis can be represented after angle integration by  $3j$ -symbols and radial matrix elements:

$$V_{jj'}^{lm'l'm'} = E(t) [(2l+1)(2l'+1)]^{1/2} \begin{pmatrix} l & 1 & l' \\ 0 & 0 & 0 \end{pmatrix} \begin{pmatrix} l & 1 & l' \\ -m & 0 & m \end{pmatrix} \sum_{nn'}^{N-1} b_{nj}^l b_{n'j'}^{l'} \langle f_n^l | r | f_{n'}^{l'} \rangle, \quad (11)$$

where the  $3j$ -symbols are only  $\neq 0$  for  $l' = l \pm 1$ . For the initial state the hydrogen ground state is used:  $\Psi(\vec{r}, t=0) = 1/\sqrt{\pi} e^{-r}$ . The system (9) is extremely stiff, with increasing basis size explicit time propagation methods lead to step sizes  $h$ , which are no longer acceptable. The positive eigenvalue spectrum of  $H_0$  is unrestricted upwards, with increasing basis size ever higher eigenvalues are approximated. Table 1 shows this as an example for 5 different radial basis sizes  $N$  with partial waves  $l = 0, 1, 2$ . The corresponding eigenvectors oscillate like  $e^{-iE_j t}$ . In order to sample these with sufficient accuracy, the step size must be significantly smaller than the period of oscillation of the largest eigenvalue,  $2\pi/|E_{\max}|$ . The eigenvalue spectrum of  $H_0$  also has an accumulation point at  $E = 0$ , the ratio of the magnitudes of the smallest to the largest eigenvalue approaches infinity with increasing basis size:  $|E_{\max}|/|E_{\min}| \rightarrow \infty$ , the time behavior of the solution is composed of proportions of strongly differing magnitudes. Implicit time propagation methods promise a remedy here. However, test calculations with implicit low - order methods - implicit 4th order Runge-Kutta methods and a 4th order Adams-Bashforth method in combination with a backward differentiation scheme (AB4BD4) [32] - have not led to any improvement in the stiffness problem. In [13], a numerically costly implicit predictor-corrector method of van der Houwen and Sommeijer [33] is used, which employs a Runge-Kutta method of order 7 for the corrector part. Here, several additional systems of equations must be solved per time step, which can only be handled by appropriate parallelization across multiple CPU cores. To reduce the demands on CPU resources, and in particular to avoid the matrix iterations that occur per time step in implicit propagation methods, a different approach is chosen in this work. The solution of (1) is expanded in an eigenvalue basis of the unperturbed Hamilton operator  $H_0$  and truncated above a given value  $E_{j_{\max}}$  with  $j_{\max} < N$ . The eigenvalues - and therefore the eigenfunctions - are not uniformly distributed along the energy axis, but have an accumulation point at  $E = 0$ . Figure 1 shows this, where the eigenvalues for  $H_0$  are depicted for different radial  $N$  and for two partial waves  $l = 0, 1$  respectively. It can be clearly seen that the maximum value increases sharply with increasing size of the radial basis. Also the distance between two eigenvalues with increasing energy becomes larger. Therefore, only a few eigenvalues contribute to the stiffness problem which justifies the chosen reduction approach. The eigenfunctions resulting from the diagonalization of  $H_0$  are only a linear combination of functions in a finite Sturmian basis. This reduction cancels the completeness of the finite-dimensional orthonormal basis space (5). Intuitively, the underlying assumption is, that high-energy eigenfunctions are only weakly or not at all occupied during the interaction period. This raises the question of the physical relevance of these high-energy eigenfunctions. A spectral decomposition to the regular Coulomb functions  $\Psi_c^l$ , normalized to an energy delta function, can provide the answer:

$$|s_E^l|^2 = |\langle \Psi_j^l(r) | \Psi_c^l(E, r) \rangle|^2. \quad (12)$$

**Table 1.** largest eigenvalues of the matrix (6) for different radial basis sizes  $N$  at specified angular momentum  $l$

	$N = 25$	$N = 50$	$N = 100$	$N = 200$	$N = 400$
$l = 0$	22.0204	95.4463	396.1940	1,613.2225	6,509.3875
$l = 1$	12.3387	49.8903	200.2164	801.7507	3,208.3427
$l = 2$	8.2384	31.8200	124.7067	493.3672	1,962.2317

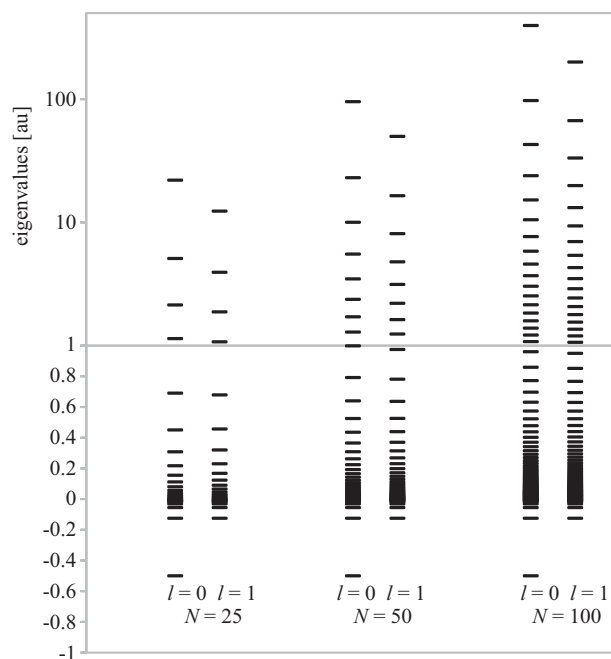


**Figure 1.** Distribution of the eigenvalues for different radial basis sizes  $N$  and specified angular momentum  $l$ , for  $E > 1$  a logarithmic scale is used; the separation between the logarithmic and linear part is depicted by the horizontal grey line

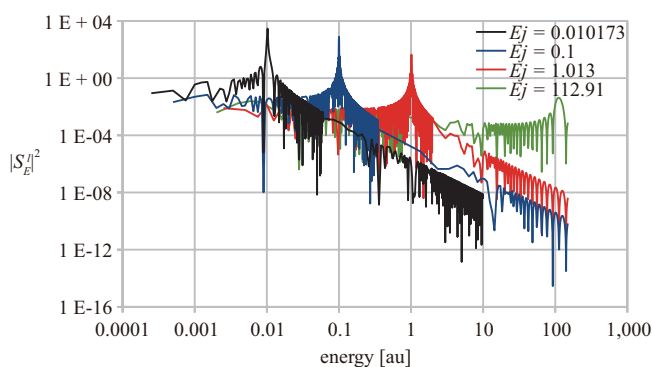


**Figure 2.** Spectral decomposition to Coulomb function for different eigenfunctions, see text below equation (12). The amplitudes  $|S_E^l|^2$  versus the energies are shown on a logarithmic scale. The eigenfunctions correspond to  $E_j = 0.010173, 0.1, 1.013$  and  $112.91$  au

Figure 2 shows the magnitude squared of the spectral amplitude  $|S_E^l|^2$  for 4 different eigenfunctions of different positive energy values in logarithmic scaling. All eigenfunctions correspond to  $l = 0$  and were calculated with radial basis size  $N = 500$ . The eigenfunctions for low positive eigenvalues are very strongly localized in Fourier space around the corresponding eigenvalue, while the eigenfunctions for high eigenvalues-here  $E_j = 112.91$ -are increasingly delocalized

and cannot be assigned to a physical continuum state. If photon energies of low frequency are considered - as here with  $\omega = 0.057$  - these high-energy eigenfunctions contribute very little in the ionization range above threshold in the kinetic energy interval  $[0, 1]$ . The main contributions in this range come from positive low-energy eigenfunctions with an accumulation point around  $E = 0$ . This justifies the approach to exclude strongly oscillating high energy eigenfunctions from the propagation. This also shows an analogy to the bound states: The low-lying eigenfunctions to negative energy represent the actual physical states very accurately, while the eigenfunctions to very small negative eigenvalues close to threshold are mathematical artifacts resulting from a Gauss-Pollaczek quadrature [8]. The cut-off value for the eigenvectors in (7) can be estimated a priori and depends on the laser parameters. At a laser frequency of  $\omega = 0.057$ , 9 photons are required for photoionization. The mean kinetic energy (ponderomotive energy) of an electron in a sinusoidal electromagnetic field is  $U_p = E_0^2 / (4\omega^2)$ . Semiclassical calculations, taking into account the Coulomb interaction, show that the kinetic energy of the electron can be up to  $3.2 U_p$  and then drops down rapidly. From this it follows that the cutoff-value  $E_{max}$  must be significantly greater than  $3.2 U_p$  in order to capture the back-scattering after ionization well and also to take into account possible temporary transitions to higher energy eigenstates during time propagation. For  $I = 5 \cdot 10^{14}$  W/cm this results in  $E_{max} \gg 3.2 U_p$  ( $= 3.5$  au).

However, this approach only takes into account the stiffness caused by  $H_0$ ; the part caused by the external field  $V(\vec{r}, t)$  is not considered. In the case of an electromagnetic pulse the interaction term  $V(\vec{r}, t)$  is not limited in either the length or velocity form and leads to further strongly oscillating components with increasing strength of the field amplitude, which make smaller stepwidths  $h$  necessary. This problem is discussed in more detail below. It should be noted that the approach (7) solves the stiffness problem as long as the external field is ‘much’ smaller than the inner atomic field strength. Test calculations for the H atom show that the influence of  $V(\vec{r}, t)$  on the stiffness increases for peak intensities greater than  $5 \cdot 10^{14}$  W/cm<sup>2</sup>.

Next, the CAP and its  $L^2$  adaptation are presented.

## 2.2 Complex absorbing potential and its $L^2$ representation

In contrast to [9], where for the absorption at the boundary in the  $L^2$  function space the Coulomb asymptotics is explicitly embedded in the system of equations via boundary conditions, this work dispenses with this approach and inserts a CAP term directly into the Hamilton operator. The CAP method is independent of the specific asymptotics and requires much less computing power. By default, the CAP acts as a boundary term in the configuration space and is an anti-hermitian operator that leads to a dissipation of probability to the ‘outside’ - the probability  $|\Psi|^2$  in the finite configuration space decreases. The absorption is frequency-selective and prevents outgoing waves from being reflected at the edge and scattered back into the interior. The width of this absorption layer must be sufficiently large - it should be at least half the wavelength of the absorbed frequency. Conversely, this means that low frequencies close to 0 are hardly attenuated at all, so the configuration space or the  $L^2$  function space should be large enough to ensure that low-frequency components of the solution, that are not detected by the CAP, do not reach the edge during propagation. The width of the absorption layer is one parameter that can be used to influence the absorption behavior; another essential parameter is the exact shape of the CAP. Polynomial terms as well as exponential approaches or combinations of both are used here. An overview of CAP approaches specifically for few cycle strong field interaction can be found in [34], although this is limited to the one-dimensional case. In almost all papers, the CAP term is placed at the boundary in the configuration space; in contrast, this work uses a modified version that operates at the boundary in the  $L^2$  function space:

$$W_{nn'}^{ll'} = \begin{cases} \langle f_n^l | \sum_i \alpha_i r^i e^{-s_i r} | f_{n'}^l \rangle \delta_{ll'} & \forall n, n' \in [N-B] \\ 0 & \text{else.} \end{cases} \quad (13)$$

The matrix expression  $W_{nn'}^{ll'}$  is 0 if one of the basis functions lies in the inner range either if  $n$  or  $n' < [N-B]$  and is of polynomial-exponential form if the radial index  $n$  and  $n'$  is in an interval specified by the integer  $B$  at the  $L^2$  boundary  $N$ .  $\alpha_i$  and  $s_i$  are freely selectable parameters that allow further optimization in addition to the coupling constant  $\eta$ . The

basis functions  $f_n^l$  are delocalized in the configuration space and cover a larger radial range, their maximum is  $\sim 2n/\xi$ . This means that the absorption layer is already wide enough even for one function with  $n = N - 1$  to absorb frequencies whose wavelength correlates with the corresponding extension. The interval width  $B$  can be used to further control the range of this absorbing layer and thus also the absorption frequencies that fit into this domain. The matrix elements (13) can be evaluated analytically, are time-independent, and do not require knowledge of values from previous time steps, i.e. these only need to be calculated once. In all calculations in this paper, the width of the absorption layer was set to  $B = 1$ , so only  $W_{N-1N-1}^l \neq 0$ . The corresponding transformation to the basis of the eigenvectors is thus reduced to:

$$W_{jj'}^{ll} = \langle \Psi_j^l | W | \Psi_{j'}^l \rangle = b_{N-1j}^l b_{N-1j'}^l \langle f_{N-1}^l | W | f_{N-1}^l \rangle. \quad (14)$$

The CAP thus couples to all eigenvectors-including those with negative energy-but only those eigenvectors, whose coefficient  $b_{N-1j}^l$  at the  $L^2$  boundary is noticeably different from 0, contribute to the absorption.

### 2.3 Time propagation

An explicit 5th order Adams-Bashforth propagation method is used to solve the coupled system of equations (9) in the reduced eigenvector basis (8):

$$\begin{aligned} \frac{dy}{dt} &= f(t, y), \\ y_{i+1} &= y_i + \frac{h}{720} [1901f(t_i, y_i) - 2774f(t_{i-1}, y_{i-1}) + 2616f(t_{i-1}, y_{i-2}) \\ &\quad - 1274f(t_{i-3}, y_{i-3}) + 251f(t_{i-4}, y_{i-4})]. \end{aligned} \quad (15)$$

In contrast to one-step methods such as Runge-Kutta, Adams-Bashforth methods are multi-step methods with a constant step size. The great advantage is that only one matrix-vector multiplication has to be performed per time step-in contrast to  $n$  for a Runge-Kutta method of order  $n$ . However, Runge-Kutta methods generally exhibit better stability. The stability behaviour is characterized by the stability function  $R(z)$ ; in the case of linear multistep methods such as Adams-Bashforth, this is a polynomial in the complex variable  $z = E_{jmax}h$ , where  $E_{jmax}$  characterizes the largest eigenvalue in terms of magnitude. In Runge-Kutta methods, the stability function is a fractional-rational function of  $z$  and generally has a larger stability range, see also [13, 35, 36]. If the external field and the CAP are ignored in  $H = H_0 + V - i\eta W$  and only the eigenvector with the highest eigenvalue in terms of magnitude is considered, the system of equations (9) is reduced to

$$\frac{d}{dt} a_{jmax} = -iE_{jmax} a_{jmax}. \quad (16)$$

The stability function is then given by

$$\Psi(t_{n+1}) = R(z)\Psi(t_n). \quad (17)$$

The relationship (17) is not only valid for the case considered here; in the general case of coupled equations, the variable  $z$  is then a non-linear function of the eigenvalues:  $z = z(E_j, h)$ . To ensure that the solution  $\Psi(t)$  remains finite in

the asymptotic limit, the following must apply:  $R(z) \leq 1$ . This condition determines the stability range and thus also the step size. The TDSE without CAP term is norm-preserving, so the following must also apply:

$$|\Psi(t_{n+1})| = |R(z)\Psi(t_n)| = |R(z)| |\Psi(t_n)|. \quad (18)$$

This results in a further condition for the stability function:  $|R(z)| = 1$ . In the reduced eigenbasis for  $H_0$ , the oscillation period  $T \sim 2\pi/E_{jmax}$ , in order to be able to sample this time interval with sufficient accuracy, the step size must be significantly smaller than  $T$ ,  $h < T$ . Test calculations for  $H_0$  confirm this. This changes when the external field is added. The dipole operator (3) has infinite range, the eigenvalues of the interaction matrix have no upper bound and increase with increasing basis. The electric field amplitude  $E_0$  of the laser can be interpreted as a coupling parameter that drives the eigenvalues of the matrix  $(H_0 + V)_{jj'}$  upwards with increasing basis size and increasing  $E_0$ . As a result, the approach (7) reduces the stiffness problem as long as the external field is considered as a perturbation to  $H_0$ , but fails at high field strengths. This also has an effect on the stability function:  $|R(z)|$  becomes greater than 1 and results in  $|\Psi| \rightarrow \infty$ , i.e. the stability range  $R(z)$  changes and the step size must be reduced. The question of how the field amplitude  $E_0$  influences the step size, is examined below. The CAP also has an effect on the stability function: The CAP is an anti-hermitian term that operates at the border of the function space and causes the norm-preserving property of the TDSE to be lost, the probability decreases:  $|\Psi(t_{n+1})| < |\Psi(t_n)|$ . The CAP therefore leads to a ‘slight’ improvement in stability. To summarize: The selected approach in a reduced eigenbasis solves the stiffness problem caused by  $H_0$  as long as the external field is ‘small’, but with increasing intensity of the external field, the stability function changes, resulting in smaller step sizes.

## 2.4 Observables

The numerical solution of the TDSE initially only provides the expansion coefficients in (7). The observables must then be extracted from these values. The occupation probabilities for Rydberg states are directly given by the corresponding coefficients in the eigenvector basis:  $a_{E_j} a_{E_j}^*$  where  $E_j \equiv (nlm)$  symbolizes the principal, angular momentum and magnetic quantum number. Ionization spectra can be calculated as the superposition of Coulomb waves  $\Psi_k^-$  to positive energy  $E = k^2/2$ :

$$\Psi(\vec{r}, t) = \int k^2 dk d\Omega_k b_{\vec{k}} \Psi_{\vec{k}}^-, \quad b_{\vec{k}} = \sum_{lm} c_E^{lm} Y_{lm}(\hat{k}), \quad (19)$$

where the vector-valued coefficient  $b_{\vec{k}}$  can be represented as a sum over spherical harmonics  $Y_{lm}(\hat{k})$  for the angular component of the momentum and scalar functions  $c_E^{lm}$  for the energy component [9]. The partial wave expansion of  $\Psi_{\vec{k}}^-$  leads to:

$$\Psi_{\vec{k}}^- = \frac{1}{kr} \sum_{lm} i^l Y_{lm}^*(\hat{k}) Y_{lm}(\hat{r}) e^{-i\sigma_l} \Psi_c^l(E, r). \quad (20)$$

The normalization is performed on incoming wave boundary conditions, which are used to describe photoionization processes. Here  $\Psi_c^l(E, r)$  is a regular Coulomb function,  $\sigma_l = \arg(\Gamma(l+1 - iz/k))$  the Coulomb phase.  $\Psi_c^l$  can in turn be represented in the Sturmian basis  $f_n^l$  [37]:

$$\Psi_c^l(E, r) = |\Psi_0^{-l}| \sum_{n=0}^{\infty} \frac{n! (2l+1)!}{(n+2l+1)!} P_n^l(E, \xi) \left[ \frac{f_n^l}{N_n^l} - \frac{f_{n-1}^l}{N_{n-1}^l} \right]. \quad (21)$$

The Pollaczek polynomials  $p_n^l$  occurring therein are energy-dependent, the analytical representation as well as to  $\Psi_0^{-l}$  can be found in [37]. With (19)-(21) the angle-integrated ionization spectrum, differential in energy, can be calculated:

$$\frac{dP}{dE} = \sum_{lm} c_E^{l,m} c_E^{lm*}. \quad (22)$$

The spectral coefficients  $c_E^{lm}$  for the partial wave  $l$  are obtained as a triple sum over Pollaczek polynomials and the eigenvectors [9]:

$$c_E^{lm} = (-1)^l e^{i\sigma_l} |\Psi_0^{-l}| \frac{\xi}{2} \frac{1}{\xi^2} \sum_{j=0}^{jmax} d_j^{lm} \sum_{n=0}^{N-1} \left(n+l+1 - \frac{2z}{\xi}\right) p_n^l(E, \xi) \sum_{n'=n}^{N-1} b_{n'j}^l N_{n'}^l. \quad (23)$$

The sums occurring therein are finite, the Pollaczek polynomials for the energy  $E$  can be calculated numerically stable via a three-term recursion formula [37]. Both, the ionization spectrum and the excitation spectrum, are CEP-dependent and periodic in the CEP-phase  $\phi$ :  $P(\phi) = P(\phi + \pi)$  [38].

## 2.5 Numerical realization

The calculation of the dipole matrix, CAP elements and eigenvectors can be carried out before the actual time propagation and are therefore available for a large number of program runs with different field parameters. The same value of the scaling parameter  $\xi = 0.9$  was used for all partial waves. This allows Rydberg states with a principal quantum number up to  $n = 30$  to be resolved for a radial basis with  $N = 500$  at angular momentum  $l = 0$ . At higher angular momentum, the accuracy decreases for the same basis size. The matrix for  $H_0$  is diagonal, the dipole matrix  $V_{jj'}^{ll'}$  is only different from zero for  $l' = l \pm 1$  and the CAP matrix  $W$  is diagonal in  $l$ . This results in a tridiagonal matrix structure in angular momentum space. The Adams-Bashforth propagation method was chosen to minimize the CPU runtime; only one matrix-vector multiplication is necessary per time step, which is also tridiagonal in the indices ( $ll'$ ) and thus further reduces the number of floating point operations. These scale approximately  $N * N * 3 * lmax$  with a total matrix size of dimension  $N * lmax$  ( $lmax$ : maximum number of partial waves included). The Adams-Bashforth method is explicit; there are no further matrix iterations per time step as with implicit methods. However, increasing amplitudes of the external field require smaller step sizes, but these are acceptable for the laser intensities considered here, as no further systems of equations need to be solved per time step. The implementation was programmed using Java, for the calculation of the eigenvectors a program library (Apfloat) was used, which allows a user-defined accuracy, the time propagation with Adams-Bashforth was carried out using the data type 'double'. The arrays required in time step  $t_{n+1}$  from the previous time step  $t_n$  can be get by simply switching array pointers and do not require mass data to be copied in the main memory. The runtime of the propagation with  $N = 700$ ,  $lmax = 50$  with a laser interaction time  $T_f = 1110$  au required about 30 hours on a computer with Intel-I9-13900 processor and 64 GB main memory.

## 3. Results

In this section, the numerical results obtained from test calculations are analyzed first. For this purpose, the damping behavior of the CAP term is examined, the dependence of the time propagation step size on the strength of the electric field, followed by illustrations of the convergence behavior as a function of the radial basis size  $N$  and the maximum number of partial waves. The method is then applied to excitation processes in laser fields: Ionization and subsequent backscattering with excitation into Rydberg states in the strong field regime and intermediate regime.

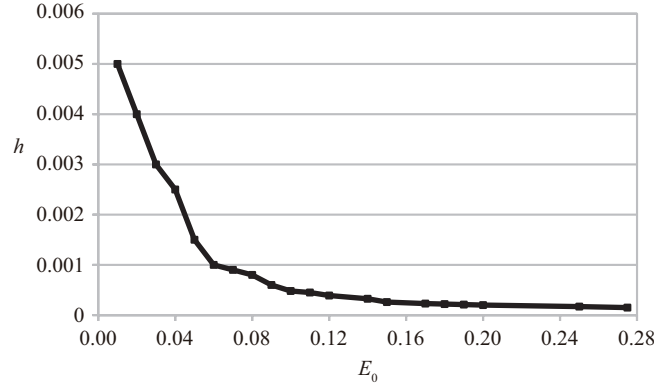


**Figure 3.** Stepwidth  $h$  versus electric field amplitude  $E_0$ . Calculations were performed without the CAP term and with a pure 3-cycle field  $E(t) = E_0 \sin(\omega t)$ , duration  $T_f = 330$  au, basis size  $N = 600$  and 50 partial waves, eigenvectors with eigenvalues  $E_j > 100$  had been excluded. Shown is the largest stepwidth, for which the norm of the wavefunction is conserved

In all calculations - with the exception of Figure 3 - a constant CAP term  $W = 1$  is used with coupling constant  $\eta = 4$ . All eigenvectors with eigenvalues  $< 100$  au were included in the expansion (7). Calculations on excitation distributions were carried out with pulses of different electric field strengths in the range  $[0.0533 - 0.12]$ . The ponderomotive energy,  $U_p = E_0^2 / (4\omega^2)$ , results for  $E_0 = 0.12$  and frequency  $\omega = 0.057$  to  $U_p = 1.11$ . This means that the cutoff value for the eigenvectors is approximately 100 times higher than  $U_p$ . Backscattering processes in the Coulomb field after transition to the continuum ( $U_p < 3.2$ ) and above threshold absorption are thus sufficiently represented, at least in terms of energy. For  $E_0 = 0.12$ , this results in a quiver amplitude of 37 au. However, the radial excursion in few cycle fields can far exceed this value. For the calculation of the Rydberg spectrum,  $N = 500$  and  $N = 600$  were used as the radial basis size. With the scaling parameter  $\xi = 0.9$ , spatial areas up to approx. 1200 au ( $N = 500$ ) and 1400 au ( $N = 600$ ) can be recorded. This should ensure that the calculations provide valid results for the phenomena under consideration.

In all presentations the  $1s$  state of atomic H is used as the initial state.

### 3.1 Complex absorbing potential

To assess the absorption behavior of the CAP term, test calculations were carried out with different potential forms - constant, quadratic, exponential:

$$W_{N-1}^l = \langle f_{N-1}^l | \mathbf{1} | f_{N-1}^l \rangle, \langle f_{N-1}^l | (\xi r)^2 | f_{N-1}^l \rangle, \langle f_{N-1}^l | e^{-\xi r} | f_{N-1}^l \rangle. \quad (24)$$

As a result there are no significant differences in the absorption behavior of the individual potential forms, so only the constant CAP is considered below. Figure 4 shows the probability integrated over the reduced function space  $|\Psi(t = T_f)|^2$  as a function of the coupling constant  $\eta$  after interaction of a one cycle laser field with frequency  $\omega = 0.057$ ,  $T_f = 110$ , and field amplitude  $E_0 = 0.1$ . A maximum absorption occurs at  $\eta \sim 4$ , calculations with other basis sizes and field strengths give a similar picture. The dependence of the probability is analogous to the use of the CAP in the calculation of resonance states [39, 40]. Figure 5 shows a more detailed insight into the attenuation behavior at  $\eta = 4$ . There the temporal development of the probability in the time interval of an oscillation period of the same frequency  $\omega = 0.057$  as in Figure 4 is plotted. The time course of the electric field  $E(t)$  is shown in the inset in Figure 5. After passing through the maximum in the 1st half-wave, the probability begins to drop at  $t \sim 37$ , where high-energy electrons reach the border in the function space and absorption by the CAP term begins. The electric field crosses the zero point at the time  $t = 55$  and then inverts its direction. For the low-energy electrons released in the 1st half-wave this leads to a reversal of motion with acceleration back to the nucleus. The weakening of the probability drop in the 2nd half-wave can be seen in the range  $[60, 90]$ . After that, the probability decreases further - electrons increasingly hit the edge and are absorbed.

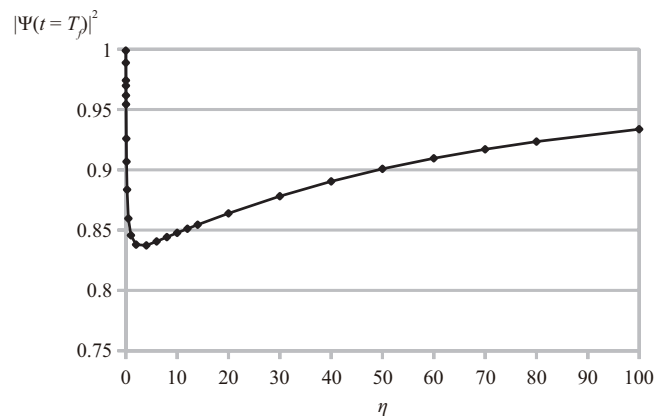


**Figure 4.** Probability  $|\Psi(t = T_f)|^2$  after passage of a one cycle pulse  $E(t) = E_0 \sin(\omega t)$  as a function of the CAP coupling strength parameter  $\eta$  ( $\omega = 0.057$ ,  $E_0 = 0.1$ , basis size  $N = 100$ ,  $lmax = 40$ )

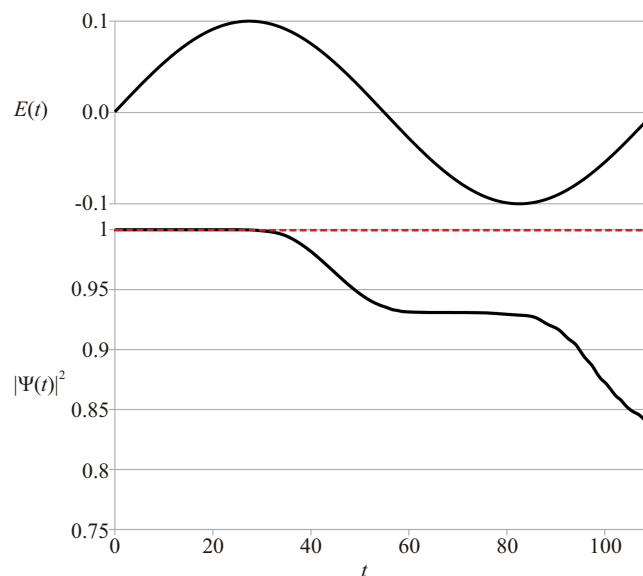


**Figure 5.** Probability  $|\Psi(t)|^2$  during interaction with a one cycle pulse  $E(t) = E_0 \sin(\omega t)$ ,  $E_0 = 0.1$ ,  $\omega = 0.057$ , CAP coupling strength  $\eta = 4$ . The upper picture shows the course of the electric field. The red dotted curve shows the probability  $|\Psi(t)|^2$  without a CAP-the norm conserving character of the TDSE is clearly manifested

### 3.2 Stiffness and stepwidth

In the theoretical section, the question was raised, as to how the intensity of the laser field affects the stiffness. This will be examined in more detail here.

The field amplitude  $E_0$  can be regarded as a coupling parameter that shifts the eigenvalues of the Hamilton matrix to larger values.

The dipole operator in both, length and velocity form, has an infinite range, the spectrum is unlimited upwards. Increasing field strengths lead to an increase in the oscillating components in the wave function caused by the dipole matrix - the system of equations becomes increasingly stiff and requires smaller step sizes in the time propagation. This can be seen in Figure 3, where the step size is plotted against the peak field amplitude  $E_0$ . Figure 3 is based on calculations with a pure 3-cycle pulse  $\omega = 0.057$ , duration 330 au, without envelope:  $E(t) = E_0 \sin(\omega t)$ , radial basis size  $N = 600$  per partial wave, maximum number of partial waves  $lmax = 50$ . The underlying basis was truncated for eigenvectors

with eigenvalues  $E_j > 100$ . As an estimate, the smallest oscillation period is  $T \sim 2\pi/100 \sim 0.063$ . In order to scan this time interval with sufficient accuracy, a step size significantly shorter must be considered. In order not to mask the results through the CAP term, which leads to a slight improvement in the stiffness problem as it absorbs higher-energy components, the time propagation was carried out without the CAP. This means that the norm of the wavefunction is conserved and tends towards infinity if the step size is too large. The smallest value of the step size  $h$ , for which the norm is conserved over the entire propagation interval  $[0, 330]$ , is shown in Figure 3.

The step size decreases with increasing amplitude  $E_0$ , as Figure 3 clearly shows. For example, at  $E_0 = 0.169$ , which corresponds to a peak intensity of  $10^{15}$  W/cm<sup>2</sup>, a step size of  $h = 0.00023$  is required. If, on the other hand, one takes into account that no further matrix iterations are needed per time step, as is the case with implicit methods, the runtime and accuracy achieved with this step size and this cutoff value can certainly be described as positive. The cutoff value 100 used here is set fairly high, test calculations - not presented here - show that it can be shifted further downwards, thus increasing the step size.

### 3.3 Convergence

Statements about convergence can only be made directly by extracting observables from numerical test calculations with different basis sizes, in this case the photoelectron spectrum as a function of the number of partial waves and the number of radial basis functions. For this, test runs were carried out with the vector potential (4) to enable also comparisons with other work [10]: In the following  $\omega = 0.057$ , the number of cycles  $N_c = 10$ , with total duration  $T_f = 1102$ , linear polarization and a laser peak intensity  $10^{14}$  W/cm<sup>2</sup>, which corresponds to a field amplitude  $E_0 = 0.0533$ , are used. The underlying categorisation of the interaction process into multiphoton and barrier suppression regimes - see Section 3.4 below - is roughly described by the Keldysh parameter  $\gamma$ : With a value of  $\gamma = 1.07$ , the interaction takes place in the intermediate regime, characterized by  $\gamma \sim 1$ .

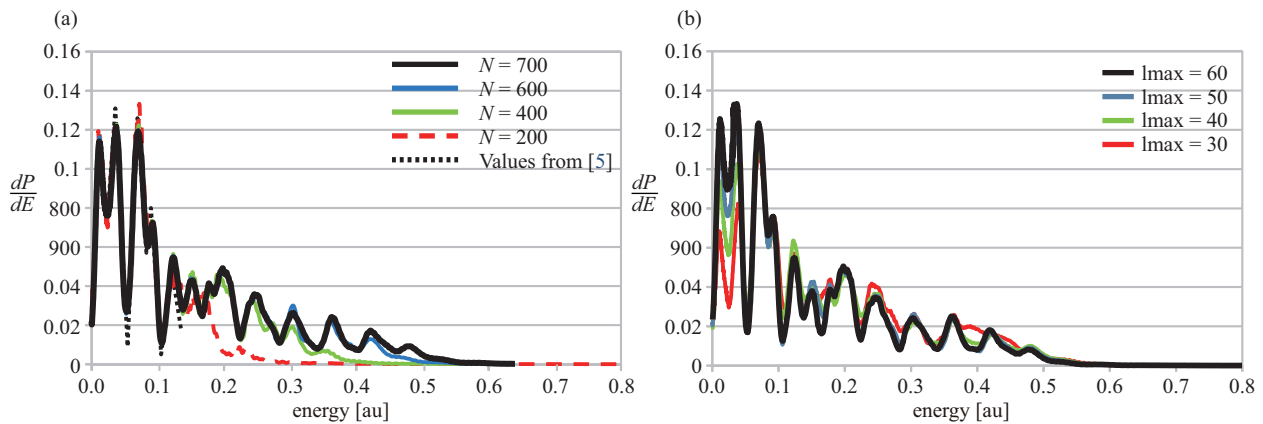


**Figure 6.** Photo electron spectrum obtained with different basis sizes. The laser field has the form (4) with  $\omega = 0.057$ ,  $E_0 = 0.0533$ ,  $\phi = 0$  and consists of 10 cycles corresponding to a total duration of  $T_f = 1102$  au. In (a) the number of radial function  $N$  is varied while the number of partial waves  $l_{\max} = 50$  was fixed. (b) shows the convergence behaviour at different  $l_{\max}$  while the number of radial function is fixed  $N = 600$

Figure 6 shows the ionization spectrum  $dP/dE$  of atomic H with the ground state as the initial state and with different radial basis sizes  $N$  (6a) and different partial waves  $l_{\max}$  (6b). In Figure 6a the calculations had been carried out with a fixed number of partial waves ( $l_{\max} = 50$ ) and different radial basis sets ranging from  $N = 200$  til  $N = 700$ . For comparison, results from [10] were included and shown by the black dotted points. The spectrum in the range  $[0, 0.1]$  is already converged for  $N = 200$ , while a much larger radial basis is required for the higher-energy spectrum ( $N = 500$  and higher). The basis with  $N = 600$  and scaling parameter  $\xi = 0.9$  scans spatial ranges up to 1400 a.u. The convergence behavior depicted in Figure 6a shows that even for moderate intensities the higher-energy components of the ionized wave

packet can penetrate into these regions up to the end of the laser pulse and require far more radial functions than for the lower energy spectrum. Figure 6b shows the convergence from the viewpoint of the number of partial waves  $l_{max}$  at constant radial basis size  $N = 600$ . Here again, it can be seen that the spectrum up to  $E = 0.15$  is already well approximated by 40 partial waves, while far more partial waves are required for the higher energy range.

### 3.4 Frustrated tunneling ionization

In the interaction of an atom with short laser pulses, however, not only ionization processes are relevant; experiments have shown [41] that a significant proportion of atoms remain in excited states. Two areas can be clearly identified here: in low-intensity fields, the Coulomb potential is only weakly deformed by the external electric field; here the interaction is well described by multiple absorption of light quanta of the frequency  $\omega$ . Resonant multiphoton transitions in Stark shifted Rydberg states lead to excitations that survive the interaction time. In this weak-field or multiphoton regime, characterized by the Keldysh parameter  $\gamma \gg 1$ , the electron is ‘heated up’ and then transitions into the continuum occur. In strong laser fields, on the other hand, the potential that the electron sees is strongly deformed by the laser electric field. The height and width fluctuates with the pulse shape of the external field - the ionization threshold is lowered or raised depending on time. In the scenario considered here, the H atom is initially in the ground state, the laser frequency is much smaller than the ionization threshold,  $\omega \ll I_p$ , so the change in the external field is slow compared to the ‘electron motion’, the electron therefore has enough time to follow the time-dependent field and adapt. For this adiabatic range, a change of perspective provides a more intuitive representation. In the time domain, the transition to the continuum can be viewed as a tunneling process. If the energy of the initial state is below the maximum of the potential barrier, the tunnel probability is highest at maximum values of the external field. The electron tunnels through the potential barrier in a small time interval around these field peaks and reaches the continuum with a low drift velocity. This is often not sufficient to counteract the external field, which inverts the field direction in the following half wave. As a result, the electronic wave packets are accelerated back to the ion body and scattered there. Low energy parts of the wavepacket can relax into field dressed Rydberg states and survive until the end of the laser pulse. This means, that a significant proportion of the tunnel electrons only occupy continuum states at intermediate times during the laser pulse, resulting in an attenuation of the ionization signal.

In very strong laser fields, the potential can also be lowered below the binding energy of the ground state; a direct transition to the continuum is thus possible: Over the Barrier Ionization. Classically, this case occurs when the electric field strength of the laser  $E_0 > Z^3/16$  (in the derivation of this condition, however, the Stark shift of the ground state is neglected; taking the Stark shift into account results in a different value [42]). The region of strong intensities - also referred to as the barrier suppression regime - includes both tunnelling through the potential barrier and over barrier ionization, and is described in the adiabatic region  $\omega \ll I_p$  by Keldysh parameter  $\gamma = \frac{\omega(2I_p)^{1/2}}{E_0}$  with  $\gamma \ll 1$ , while the multiphoton regime is characterized by  $\gamma \gg 1$ . In the intermediate region  $\gamma \sim 1$ , the dynamics is only inadequately interpreted by these two perspectives - frequency domain or time domain. Here, neither the SFA nor the perturbation-theoretical treatment within the framework of multiphoton absorption are sufficient; the exact solution of the TDSE is the method of choice here.

The dynamics in the adiabatic barrier suppression regime - and here especially the excitation spectrum after the passage of a laser pulse - is qualitatively, and partly also quantitatively, well described by the two-step model of the SFA. Investigations of this topic are currently the focus of several studies, both on the basis of SFA and TDSE [21–30]. For example Ivanov et al. [23] solve the TDSE and calculate the Rydberg distribution as a function of laser parameters such as CEP, frequency and interaction duration. Using a time-dependent correlation function, they analyze the wave function backwards in time and can thus extract the physical parameters, such as the tunnel exit time, that have led to excited states. Hu et al. [22] extend the two-stage model of the SFA with field dressed Rydberg wavefunctions and thus calculate the excitation spectrum of H and He. Liang et al. [25] and Ortmann et al. [27] investigate excitation distributions for different principal quantum numbers  $n$  and angular quantum numbers  $l$  in the area of tunnel ionization using the Classical Trajectory Monte Carlo method, whereby the influence of the number of field cycles is also investigated. Shvetsov-Shilovski et al. [28] and Olofsson et al. [26] also use the SFA to calculate the  $(n, l)$  distribution of Rydberg states. The highly oscillating integrals for calculating the transition probabilities are approximated in their work using the saddle point method.

In the following, we take up this topic and apply the  $L^2$  method presented in the theory section to calculate excitation spectra in few cycle fields and investigate the  $(n, l)$ -Rydberg occupations as a function of the laser parameters.

To test the quality of the expansion (7), we first compare the results with the values of Olofsson et al. [26]. Like the ionization spectrum, the occupation of excited states in strong few cycle fields also shows a pronounced dependence on the CEP. This applies not only to the distribution of the Rydberg states at different principal quantum numbers, but also to the angular momentum manifold within the same principal quantum number. Figure 7 shows the excitation of the Rydberg state with  $n = 5$  at different angular momentum values  $l$  as a function of the CEP. The pulse shape of the laser field is given by (4): linear polarization,  $\omega = 0.056987$ ,  $E_0 = 0.065377$  (peak intensity  $1.5 \cdot 10^{14}$  Wcm<sup>2</sup>) and  $N_c = 2$  field cycles. The values calculated within this  $L^2$  approach agree well with [26], which used a B-spline basis for the solution of the TDSE.

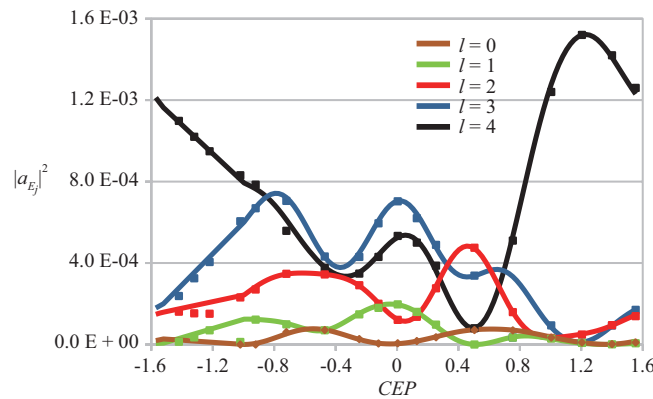


**Figure 7.** CEP-dependence of excitation of the  $n = 5$  angular momentum manifold. The laser pulse has the form (4) with  $\omega = 0.056987$ ,  $E_0 = 0.065377$  and consists of 2 cycles corresponding to a total duration of  $T_f = 220.51$  au. The rectangular symbols are taken from [26]

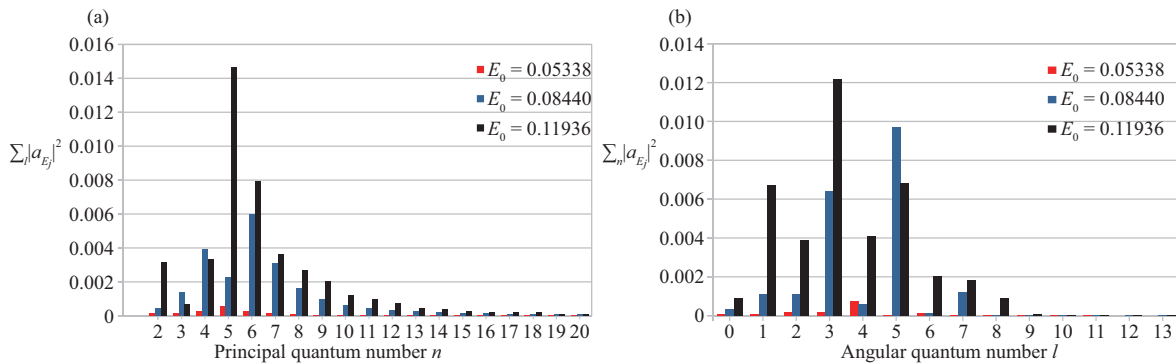


**Figure 8.** Distribution of Rydberg states after passage of a 3-cycle pulse with  $\omega = 0.057$ ,  $\phi = 0$  at different field amplitudes  $E_0$ . (a) excitation spectrum in the  $n$ -quantum numbers, whereby the angular substates within each  $n$  are summed. (b) angular momentum distribution- here the contributions from the principal quantum numbers are summed

The excitation distribution in the principal quantum number after the end of the laser pulse at different intensities is shown in Figure 8a. This is based on the field shape (4) with  $\omega = 0.057$  and 3 oscillation cycles  $N_c = 3$  and CEP  $\phi = 0$ . In (a) the angular momentum substates within the same principal quantum number  $n$  were summed. The intensities correspond to different values of the Keldysh parameter  $\gamma$ . For  $E_0 = 0.0534$  ( $\gamma = 1.069$ ), the most populated state is  $n = 5$  with a probability of 0.0005366 which agrees very well with values of [23]. The principal quantum number with maximum occupation probability can be estimated in the tunneling regime for  $\gamma < 1$ : Semiclassical calculations in the framework of SFA [27, 41] show a scaling  $n \sim E_0^{1/2}/\omega$  for few cycle pulses. For  $E_0 = 0.0844$  ( $I = 2.5 \cdot 10^{14}$  W/cm<sup>2</sup>

peak intensity)  $n = 5$  results, for  $E_0 = 0.119$  ( $I = 5 \cdot 10^{14}$  W/cm<sup>2</sup>)  $n = 6$  follows. Figure 8a shows that this behavior is not exactly met, for  $E_0 = 0.0844$  we have  $n = 6$ , while for  $E_0 = 0.119$  the most populated state is  $n = 5$ . The cause probably lies in the few-cycle pulse, which is composed of 6 half-cycles of different amplitudes, whereby only one half-wave reaches the maximum amplitude due to the  $\sin^2$  envelope. The Stark shift of the Rydberg states is also likely to play a relevant role, leading to resonance effects. Another perspective on the excitation spectrum is given by the distribution of the angular momentum states. Figure 8b shows the resolution in  $l$ -space after the end of the laser pulse at different peak intensities, whereby all  $n$ -contributions were summed. For comparability, the same laser parameters were used as in (a). As with the  $n$ -quantum numbers, it can also be seen here that the occupations have a dominant value in the angular momentum space and then fall off with increasing  $l$  for all intensities. In the tunnel region  $\gamma < 1$ , the dominant  $l_d$  value can be estimated within the framework of the SFA and semiclassical model assumptions based on classical Kepler orbits [43]:  $l_d \sim (2 E_0)^{1/2} / \omega$ . For  $E_0 = 0.0844$   $l_d = 7$  results while for  $E_0 = 0.119$   $l_d = 8$  and 9 are predicted. Figure 8b shows that these values are not met for the field parameters considered here; for  $E_0 = 0.0844$   $l_d = 5$  and for  $E_0 = 0.119$   $l_d = 3$  results. Reasons may be resonance effects in Stark shifted Rydberg states and the fact that the few-cycle field reaches the maximum amplitude only during one half-cycle.

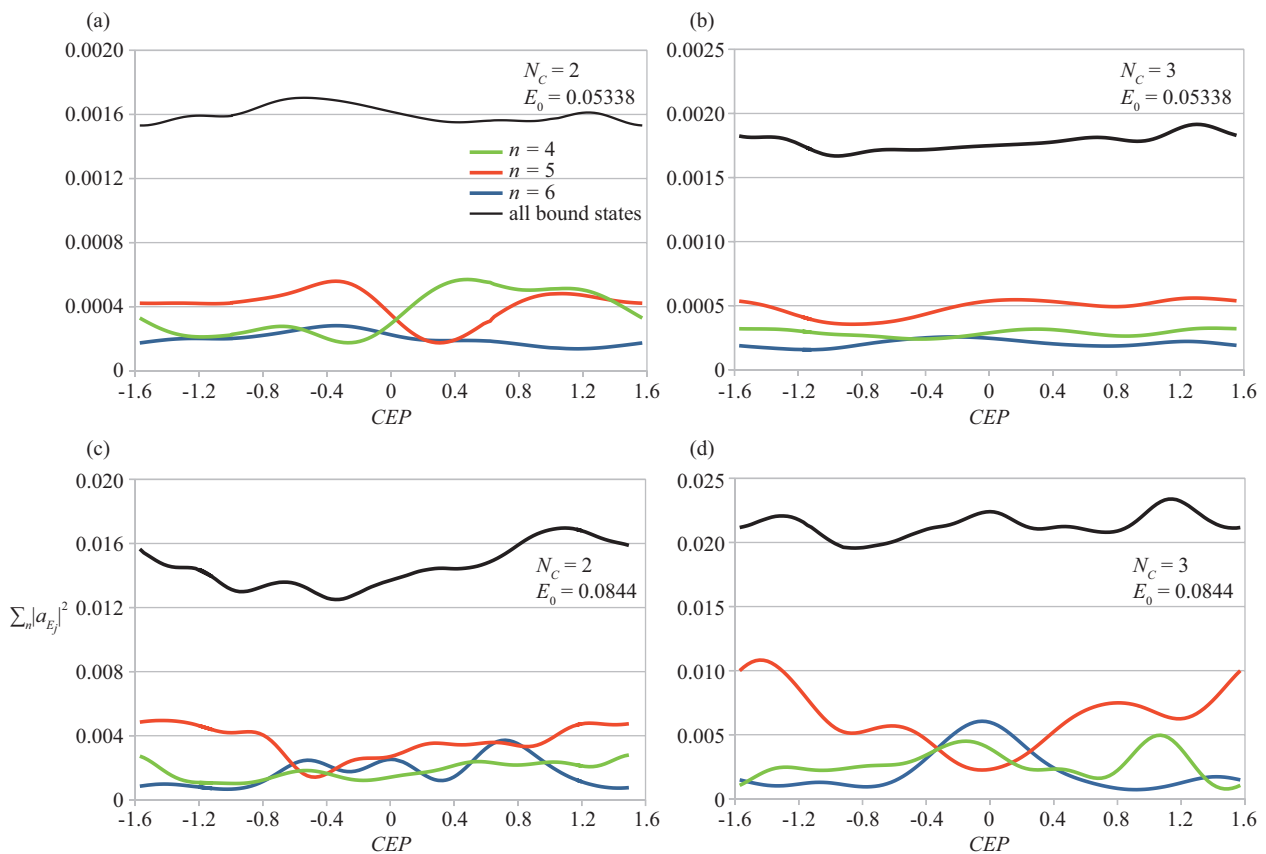


**Figure 9.** Excitation spectrum of Rydberg states  $n = 4, 5, 6$  after passage of a 2-cycle pulse ( $N_c = 2$ , left column a, c) and 3-cycle pulse (right column b, d) at field strengths  $E_0 = 0.0533, 0.0844$ . The angular momentum substates within each  $n$  are summed

The effects of CEP on the ionization spectrum have been investigated in a number of papers, see e.g. [44–48] and references therein, but there are only a few studies on the dependence of excitation spectra on CEP [26, 49]. In the following, the CEP dependence of Rydberg occupations in  $H$  in the intermediary regime as well as in the tunneling regime is examined in more detail. Figure 9 shows the excitation probabilities of Rydberg states with principal quantum number  $n = 4, 5, 6$  as a function of the CEP for a 2- and 3-cycle pulse in the intermediate regime  $\gamma = 1.069$  and in

the tunneling regime  $\gamma = 0.6754$ . The values are the sum of the angular momentum substates to a given  $n$ . As Figure 9 reveals, the occupation probability is also strongly intensity-dependent: Increasing the peak amplitude of the electric field to  $E_0 = 0.0844$  leads to an increase by a factor of almost 10. Please observe that for the bottom row ( $E_0 = 0.0844$ ) a scaling greater by a factor of 10 was used to represent the excitation probabilities. In both, the 2- and 3-cycle pulses, the occupation probabilities do not show a uniform pattern. While the excitation probability after passing a 3-cycle pulse with peak amplitude  $E_0 = 0.0533$  (b) is only slightly sensitive to the CEP, the other field parameters show a much more pronounced CEP dependence (a, c, d). The largest CEP-dependent variability results at  $n = 5$  for a 3-cycle pulse with  $E_0 = 0.0844$  (d).

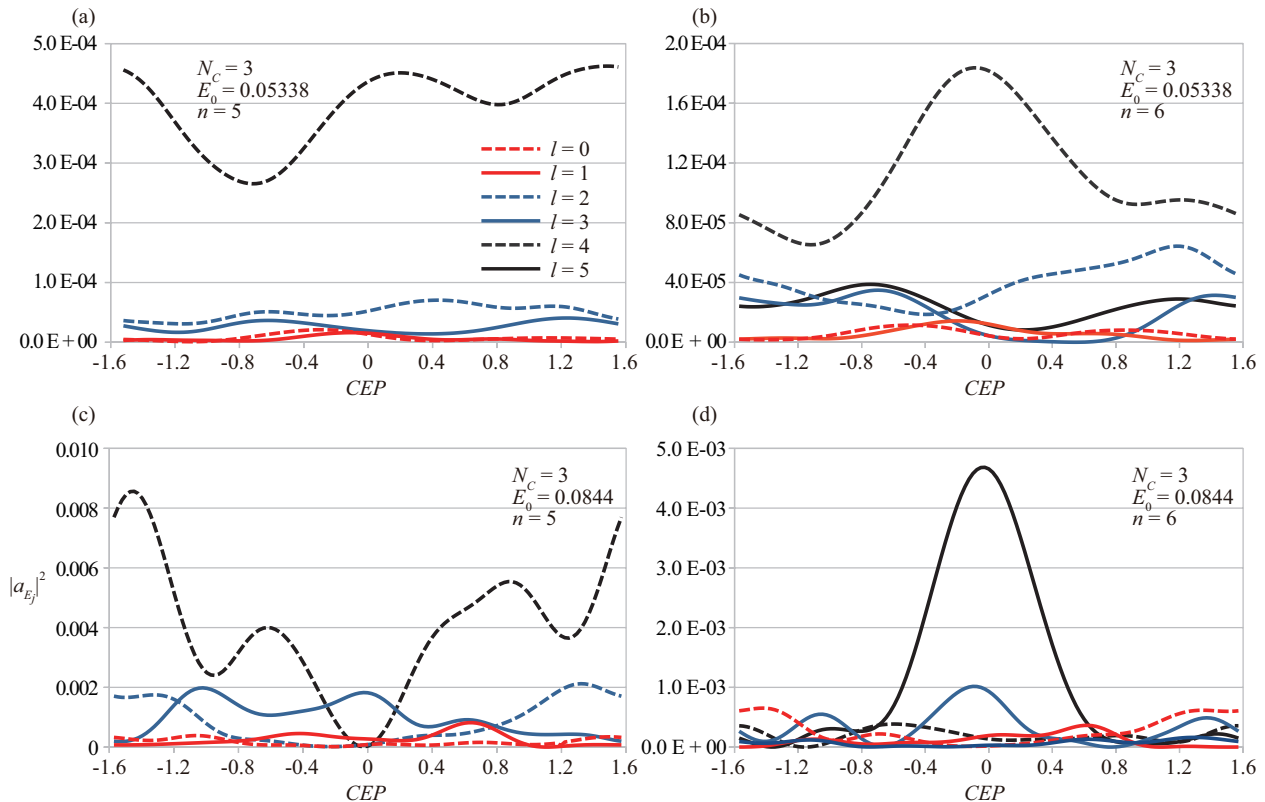


**Figure 10.** Excitation spectrum of  $n = 5$  (a, c) and  $n = 6$  (b, d) Rydberg states resolved according to the angular momentum number  $l$  after passage of a 3-cycle pulse at field strengths  $E_0 = 0.0533$  and  $E_0 = 0.0844$ . Different scalings are used for the amplitudes

A more detailed insight can be gained from the contribution of the individual angular momentum substates: Figure 10 shows the  $l$ -resolved occupation of the  $n = 5$  and  $n = 6$  Rydberg states as a function of the CEP for a 3-cycle pulse and 2 peak field amplitudes. It can be clearly seen that the different  $l$ -states are excited to different degrees, both for  $n = 5$  and  $n = 6$ . Mainly higher  $l$ -substates remain after the passage of the laser pulse, while low  $l$ -states are hardly excited in the intermediate regime as well as in the tunneling regime. In the tunneling regime at  $n = 5$  the dominant occupation is at  $l = 4$ , while at  $n = 6$  at  $l = 4$  (b) and  $l = 5$  (d). This trend towards the occupation of higher  $l$ -states is also consistent with the findings of [26].

## 4. Conclusion

The aim of the work was to develop an efficient and reliable method for solving the TDSE in strong laser fields and thus to describe the excitation after tunnel ionization.

By transforming to an eigenvector basis of the unperturbed system and eliminating strongly oscillating eigenvectors in combination with an explicit time propagation method, the stiffness problem and thus CPU resource consumption can be significantly reduced. However, the problem cannot be completely eliminated with the approach chosen here, as the stiffness caused by the external field is not captured. Test calculations carried out in this work show that the  $L^2$  spectral approach is well suited for external fields with peak intensities  $< 5 \cdot 10^{14}$  W/cm<sup>2</sup>; with higher values, the stiffness induced by the external field increases and requires increasingly smaller step sizes.

To reduce reflections caused by the finite basis, a CAP was implemented. In contrast to all other CAP applications, the CAP directly operates at the border of the  $L^2$  function space-and not in the configuration space. The attenuation of the probability density as a function of the coupling constant and the potential form was investigated: As with CAP methods operating directly in configuration space, maximum absorption occurs at a given value of the coupling constant, which changes only insignificantly with variation of the basis size. Test calculations show that the absorption behavior is only slightly influenced by the CAP shape - in contrast to CAP shapes that are placed at the border of the configuration space. The CAP positioned at the boundary of the  $L^2$  space preferentially absorbs high-energy components that correspond to short wavelengths, while absorption in the low-energy range is reduced (at longer wavelengths). The CAP thus has a stabilizing effect on the stiffness of the differential equation system. Not all aspects of the CAP were investigated in this work. Further optimizations are possible, e.g. by increasing the width of the absorption layer. In this way, the boundary of the  $L^2$  function space, in which the CAP operates, can be extended to several radial functions, thereby extending the absorption capacity to longer wavelengths.

Another aspect is the convergence behavior with respect to the radial basis and partial wave number. For converged values of the wave function in the low-energy ionization range, significantly fewer Sturmians are required than for the higher-energy ionization continuum. The ionization spectra calculated at  $I = 10^{14}$  W/cm<sup>2</sup> show good agreement with [10], which also uses a Sturmian expansion and combines it with a method based on Fatunla to reduce the stiffness problem. It should also be noted that with higher intensities ( $> 8 \cdot 10^{14}$  W/cm<sup>2</sup>) and longer interaction times  $T_f > 1,000$  au. the required partial wave number increases disproportionately ( $l_{max} > 100$ ).

As an application scenario, which is currently also being investigated in other works, the excitation spectrum of atomic H after the passage of a few cycle laser pulse was examined. The results obtained here show a very good agreement with calculations by [26], where a B-spline method is used to solve the TDSE. It is also shown that in few-cycle fields the occupation probabilities depend very sensitively on the laser parameters such as CEP and intensity; in particular - with the field parameters considered here - mainly Rydberg states with higher angular momentum values remain. This is in contrast to semiclassical approximations based on the 2-step model of the SFA, which predict Rydberg states with small angular momentum values [26].

For the calculations of the ionization and excitation spectrum, the oscillating eigenvectors were cut off above a rather high value ( $E_j > 100$ ). It was not investigated to what extent a further reduction in the cut-off value affects the observables. This opens up another possibility to further counteract stiffness.

The calculations were carried out with the Coulomb potential, other potential forms within the framework of the SAE approach can be inserted into the method presented here. The prerequisite is that the potentials are free of poles and can be represented in a Sturmian basis. This applies to all potential forms whose radial part can be expressed as sums of exponentials and powers. An extension of the reduction method presented here to describe further phenomena such as HHG or interaction with elliptically polarized laser pulses is straightforward.

## Acknowledgement

This work was supported by the University of Applied Sciences Esslingen, Germany, Grant Number: 4536302.

## Conflict of interest

The authors declare no competing financial interest.

## References

- [1] Amini K, Biegert J, Calegari F, Chacón A, Ciappina MF, Dauphin A, et al. Symphony on strong field approximation. *Reports on Progress in Physics*. 2019; 82(11): 116001. Available from: <https://doi.org/10.1088/1361-6633/ab2bb1>.
- [2] Ahmed HM. Numerical solutions of Korteweg-de Vries and Korteweg-de Vries-Burger's equations in a Bernstein polynomial basis. *Mediterranean Journal of Mathematics*. 2019; 16(4): 102. Available from: <https://doi.org/10.1007/s00009-019-1375-1>.
- [3] Ahmed HM. A new first finite class of classical orthogonal polynomials operational matrices: An application for solving fractional differential equations. *Contemporary Mathematics*. 2023; 4(4): 975. Available from: <https://doi.org/10.37256/cm.4420232716>.
- [4] Ahmed HM. New generalized Jacobi polynomial Galerkin operational matrices of derivatives: An algorithm for solving boundary value problems. *Fractal and Fractional*. 2024; 8(4): 199. Available from: <https://doi.org/10.3390/fractalfract8040199>.
- [5] Peng LY, Starace AF. Application of Coulomb wave function discrete variable representation to atomic systems in strong laser fields. *Journal of Chemical Physics*. 2006; 125(15): 154311. Available from: <https://doi.org/10.1063/1.2358351>.
- [6] Tetchou Nganso HM, Abdourama, Kwato Njock MG. Ionization of hydrogen atom driven by ultrashort intense laser pulses: Study in momentum space of phase-dependent effects. *Indian Journal of Physics*. 2024; 98(6): 1937-1950. Available from: <https://doi.org/10.1007/s12648-023-02972-w>.
- [7] Rotenberg M. Theory and applications of Sturmian functions. *Advances in Atomic and Molecular Physics*. 1970; 6: 233-268. Available from: [https://doi.org/10.1016/S0065-2199\(08\)60206-7](https://doi.org/10.1016/S0065-2199(08)60206-7).
- [8] Alhaidari AD, Heller EJ, Yamani HA, Abdelmonem MS. *The J-Matrix Method*. Dordrecht: Springer; 2010.
- [9] Gersbacher R, Broad JT. J-Matrix time propagation of atomic hydrogen in attosecond field. *Scientific Reports*. 2022; 12: 11155. Available from: <https://doi.org/10.1038/s41598-022-14706-9>.
- [10] Madroñero J, Piraux B. The dynamics of the ionization of atoms exposed to strong low-frequency fields. *Journal of Physics: Conference Series*. 2010; 212: 012027. Available from: <https://doi.org/10.1088/1742-6596/212/1/012027>.
- [11] Sumon MMI, Nurulhoque M. Comparative study of numerical methods for solving initial value problems of ordinary differential equations. *American Journal of Applied Mathematics*. 2023; 11(6): 106-118. Available from: <https://doi.org/10.11648/j.ajam.20231106.12>.
- [12] Gebregiorgis S, Gofe G. The comparison of Runge-Kutta and Adams-Bashforth Moulton methods for the first order ordinary differential equations. *International Journal of Current Research*. 2016; 8: 27356-2736.
- [13] Huens E, Piraux B, Bugacov A, Gajda M. Numerical studies of the dynamics of multiphoton processes with arbitrary field polarization: Methodological considerations. *Physical Review A*. 1997; 55(3): 2132-2143. Available from: <https://doi.org/10.1103/PhysRevA.55.2132>.
- [14] Frapiccini A, Hamido A, Schröter S, Pyke D, Mota-Furtado F, O'Mahony PF, et al. Explicit schemes for time propagating many-body wave functions. *Physical Review A*. 2014; 89(2): 023418. Available from: <https://doi.org/10.1103/PhysRevA.89.023418>.
- [15] Fatunla S. Numerical integrators for stiff and highly oscillatory differential equations. *Mathematics of Computation*. 1980; 34(150): 373-390. Available from: <https://doi.org/10.2307/2006091>.
- [16] Nyengeri H, Ndenzako E, Nizigiyimana R. The explicit Fatunla's method for first-order stiff systems of scalar ordinary differential equations: Application to Robertson problem. *Open Access Library Journal*. 2019; 6(4): 1-15. Available from: <https://doi.org/10.4236/oalib.1105291>.
- [17] Miyagi H, Madsen LB. Exterior time scaling with the stiffness-free Lanczos time propagator: Formulation and application to atoms interacting with strong midinfrared lasers. *Physical Review A*. 2016; 93(3): 033420. Available from: <https://doi.org/10.1103/PhysRevA.93.033420>.
- [18] Tao L, Scrinzi A. Photo-electron momentum spectra from minimal volumes: The time-dependent surface flux method. *New Journal of Physics*. 2012; 14: 013021. Available from: <https://doi.org/10.1088/1367-2630/14/1/013021>.
- [19] Scrinzi A. Infinite-range exterior complex scaling as a perfect absorber in time-dependent problems. *Physical Review A*. 2010; 81(5): 053845. Available from: <https://doi.org/10.1103/PhysRevA.81.053845>.
- [20] Yamani HA, Abdelmonem MS. The complex-scaling method using a complete  $L^2$ -basis. *Journal of Physics A: Mathematical and General*. 1996; 29: 6991. Available from: <https://doi.org/10.1088/0305-4470/29/21/029>.

- [21] Piraux B, Mota-Furtado F, O'Mahony PF, Galstyan A, Popov YV. Excitation of Rydberg wave packets in the tunneling regime. *Physical Review A*. 2017; 96(4): 043403. Available from: <https://doi.org/10.1103/PhysRevA.96.043403>.
- [22] Hu S, Hao X, Lv H, Liu M, Yang T, Xu H, et al. Quantum dynamics of atomic Rydberg excitation in strong laser fields. *Optics Express*. 2019; 27(22): 31629-31643. Available from: <https://doi.org/10.1364/OE.27.031629>.
- [23] Ivanov IA, Kheifets AS, Kim KT. Correlation analysis of frustrated tunneling ionization. *Physical Review A*. 2023; 107(4): 043106. Available from: <https://doi.org/10.1103/PhysRevA.107.043106>.
- [24] Li Q, Tong X, Morishita T, Wei H, Lin CD. Rydberg states in the strong field ionization of hydrogen by 800, 1,200 and 1,600 nm lasers. *Journal of Physics B: Atomic, Molecular and Optical Physics*. 2014; 47: 204019. Available from: <https://doi.org/10.1088/0953-4075/47/20/204019>.
- [25] Liang J, Zhang R, Ma X, Zhou Y, Lu P. Angular momentum distribution in strong-field frustrated tunneling ionization. *Chinese Optics Letters*. 2018; 16(4): 040202. Available from: <https://doi.org/10.1364/COL.16.040202>.
- [26] Olofsson E, Carlström S, Dahlström JM. Frustrated tunneling dynamics in ultrashort laser pulses. *Journal of Physics B: Atomic, Molecular and Optical Physics*. 2021; 54(15): 154002. Available from: <https://doi.org/10.1088/1361-6455/ac1ae4>.
- [27] Ortmann L, Hofmann C, Ivanov IA, Landsman AS. Controlling quantum numbers and light emission of Rydberg states via the laser pulse duration. *Physical Review A*. 2021; 103(6): 063112. Available from: <https://doi.org/10.1103/PhysRevA.103.063112>.
- [28] Shvetsov-Shilovski NI, Goreslavski SP, Popruzhenko SV, Becker W. Capture into Rydberg states and momentum distributions of ionized electrons. *Laser Physics*. 2009; 19: 1550-1558. Available from: <https://doi.org/10.1134/S1054660X09150377>.
- [29] Venzke J, Reiff R, Xue Z, Jaroń-Becker A, Becker A. Angular momentum distribution in Rydberg states excited by a strong laser pulse. *Physical Review A*. 2018; 98(4): 043434. Available from: <https://doi.org/10.1103/PhysRevA.98.043434>.
- [30] Xu J, Zhou Y, Li Y, Liu A, Chen Y, Ma X, et al. Dynamics of frustrated tunneling ionization driven by inhomogeneous laser fields. *New Journal of Physics*. 2022; 24: 123043. Available from: <https://doi.org/10.1088/1367-2630/acadfe>.
- [31] Ambrosio MJ, Del Punta JA, Rodriguez KV, Gasaneo G, Ancarani LU. Mathematical properties of generalized Sturmian functions. *Journal of Physics A: Mathematical and Theoretical*. 2011; 45: 015201. Available from: <https://doi.org/10.1088/1751-8113/45/1/015201>.
- [32] Cox SM, Matthews PC. Time differencing for stiff systems. *Journal of Computational Physics*. 2002; 176(2): 430-455. Available from: <https://doi.org/10.1006/jcph.2002.6995>.
- [33] Van der Houwen PJ, Sommeijer BP. Iterated Runge-Kutta methods on parallel computers. *SIAM Journal on Scientific and Statistical Computing*. 1991; 12(5): 1000-1028. Available from: <https://doi.org/10.1137/0912054>.
- [34] Yu Y, Esry BD. An optimized absorbing potential for ultrafast, strong-field problems. *Journal of Physics B: Atomic, Molecular and Optical Physics*. 2018; 51: 095601. Available from: <https://doi.org/10.1088/1361-6455/aab5d6>.
- [35] Hosea ME, Shampine LF. Efficiency comparisons of methods for integrating ODEs. *Computers & Mathematics with Applications*. 1994; 28(6): 45-55. Available from: [https://doi.org/10.1016/0898-1221\(94\)00151-0](https://doi.org/10.1016/0898-1221(94)00151-0).
- [36] Najmuddin A, Charan S. Numerical accuracy between Runge-Kutta Fehlberg method and Adams-Bashforth method for first order ordinary differential equations with boundary value. *Journal of Mathematics and Computer Science*. 2016; 6(6): 1145-1156. Available from: <https://doi.org/10.32628/IJSRSET196142>.
- [37] Broad JT. Calculation of two-photon processes in hydrogen with an  $L^2$  basis. *Physical Review A*. 1985; 31(3): 1494-1514. Available from: <https://doi.org/10.1103/PhysRevA.31.1494>.
- [38] Roudnev V, Esry BD. General theory of carrier-envelope phase effects. *Physical Review Letters*. 2007; 99: 220406. Available from: <https://doi.org/10.1103/PhysRevLett.99.220406>.
- [39] Gyamfi JA, Jagau TC. A new strategy to optimize complex absorbing potentials for the computation of resonance energies and widths. *Journal of Chemical Theory and Computation*. 2024; 20(3): 1096-1107. Available from: <https://doi.org/10.1021/acs.jctc.3c01039>.
- [40] Satyabrata S, Ho YK. The complex absorbing potential method (CAP) to study the Stark effect in hydrogen and lithium. *Journal of Physics B: Atomic, Molecular and Optical Physics*. 2000; 33(12): 2195. Available from: <https://doi.org/10.1088/0953-4075/33/12/303>.
- [41] Nubbemeyer T, Gorling K, Saenz A, Eichmann U, Sandner W. Strong-field tunneling without ionization. *Physical Review Letters*. 2008; 101(23): 233001. Available from: <https://doi.org/10.1103/PhysRevLett.101.233001>.

- [42] Mulser P, Bauer D. *High Power Laser-Matter Interaction*. Berlin: Springer; 2010.
- [43] Arbó DG, Dimitriou KI, Persson E, Burgdörfer J. Sub-Poissonian angular momentum distribution near threshold in atomic ionization by short laser pulses. *Physical Review A*. 2008; 78(1): 013406. Available from: <https://doi.org/10.1103/PhysRevA.78.013406>.
- [44] Nakajima T, Watanabe S. Effects of the carrier-envelope phase in the multiphoton ionization regime. *Physical Review Letters*. 2006; 96(21): 213001. Available from: <https://doi.org/10.1103/PhysRevLett.96.213001>.
- [45] Wallace WC, Pullen MG, Laban DE, Ghafur O, Xu H, Palmer AJ, et al. Carrier-envelope phase effects in above-threshold ionization of atomic hydrogen. *New Journal of Physics*. 2013; 15: 033002. Available from: <https://doi.org/10.1088/1367-2630/15/3/033002>.
- [46] Kang KS, Kim K, Lee JH, Lee J, Kim CM, Nam CH. Carrier-envelope-phase-dependent above-threshold ionization of xenon observed with multi-cycle laser pulses. *Optics Express*. 2014; 22(3): 3684-3690. Available from: <https://doi.org/10.1364/OE.22.003684>.
- [47] Peng LY, Pronin EA, Starace AF. Attosecond pulse carrier-envelope phase effects on ionized electron momentum and energy distributions: Roles of frequency, intensity and an additional IR pulse. *New Journal of Physics*. 2008; 10: 025030. Available from: <https://doi.org/10.1088/1367-2630/10/2/025030>.
- [48] Peng LY, Starace AF. Attosecond pulse carrier-envelope phase effects on ionized electron momentum and energy distributions. *Physical Review A*. 2007; 76(4): 043401. Available from: <https://doi.org/10.1103/PhysRevA.76.043401>.
- [49] Chetty D, Glover RD, Tong XM, deHarak BA, Xu H, Haram N, et al. Carrier-envelope phase-dependent strong-field excitation. *Physical Review Letters*. 2022; 128(17): 173201. Available from: <https://doi.org/10.1103/PhysRevLett.128.173201>.